

Compared discharge characteristics and film modifications of atmospheric pressure plasma jets with two different electrode geometries

Xiong Chen(陈雄), Xing-Quan Wang(王兴权), Bin-Xiang Zhang(张彬祥), Ming Yuan(袁明), and Si-Ze Yang(杨思泽)

Citation: Chin. Phys. B, 2023, 32 (**11**): 115201. DOI: 10.1088/1674-1056/ace768
Journal homepage: http://cpb.iphy.ac.cn; http://iopscience.iop.org/cpb

What follows is a list of articles you may be interested in

Influence of oxygen addition on the discharge characteristics of an argon plasma jet at atmospheric pressure

Junyu Chen(陈俊宇), Na Zhao(赵娜), Jiacun Wu(武珈存), Kaiyue Wu(吴凯玥), Furong Zhang(张芙蓉),Junxia Ran(冉俊霞), Pengying Jia(贾鹏英), Xuexia Pang(庞学霞), and Xuechen Li(李雪辰)
Chin. Phys. B, 2022, 31 (**6**): 065205. DOI: 10.1088/1674-1056/ac601a

Sterilization of mycete attached on the unearthed silk fabrics by an atmospheric pressure plasma jet

Rui Zhang(张锐), Jin-song Yu(於劲松), Jun Huang(黄骏), Guang-liang Chen(陈光良), Xin Liu(刘欣), Wei Chen(陈维), Xing-quan Wang(王兴权), Chao-rong Li(李超荣)
Chin. Phys. B, 2018, 27 (**5**): 055207. DOI: 10.1088/1674-1056/27/5/055207

Characteristic plume morphologies of atmospheric Ar and He plasma jets excited by a pulsed microwave hairpin resonator

Zhao-Quan Chen(陈兆权), Ben-Kuan Zhou(周本宽), Huang Zhang(张煌), Ling-Li Hong(洪伶俐), Chang-Lin Zou(邹长林), Ping Li(李平), Wei-Dong Zhao(赵卫东), Xiao-Dong Liu(刘晓东), Olga Stepanova, A A Kudryavtsev
Chin. Phys. B, 2018, 27 (**5**): 055202. DOI: 10.1088/1674-1056/27/5/055202

Numerical study of the effect of water content on OH production in a pulsed-dc atmospheric pressure helium-air plasma jet

Mu-Yang Qian(钱沐杨), Cong-Ying Yang(杨从影), Zhen-dong Wang(王震东), Xiao-Chang Chen(陈小昌), San-Qiu Liu(刘三秋), De-Zhen Wang(王德真)
Chin. Phys. B, 2016, 25 (**1**): 015202. DOI: 10.1088/1674-1056/25/1/015202

Atmospheric pressure plasma jet utilizing Ar and Ar/H_2O mixtures and its applications to bacteria inactivation

Cheng Cheng (程诚), Shen Jie (沈洁), Xiao De-Zhi (肖德志), Xie Hong-Bing (谢洪兵), Lan Yan (兰彦), Fang Shi-Dong (方世东), Meng Yue-Dong (孟月东), Chu Paul K (朱剑豪)
Chin. Phys. B, 2014, 23 (**7**): 075204. DOI: 10.1088/1674-1056/23/7/075204

Compared discharge characteristics and film modifications of atmospheric pressure plasma jets with two different electrode geometries

Xiong Chen(陈雄)[1], Xing-Quan Wang(王兴权)[1,†], Bin-Xiang Zhang(张彬祥)[2], Ming Yuan(袁明)[1], and Si-Ze Yang(杨思泽)[3]

[1] *Institute of Low Temperature Plasma Technology, School of Physics and Electronic Information, Gannan Normal University, Ganzhou* 341000, *China*
[2] *The* 722 *Research Institute of CSSC, Wuhan* 430205, *China*
[3] *Institute of Physics, Chinese Academy of Sciences, Beijing* 100190, *China*

(Received 26 June 2023; revised manuscript received 11 July 2023; accepted manuscript online 14 July 2023)

Atmospheric pressure plasma jet shows great potential for polymer film processing. The electrode geometry is the key factor to determine discharge characteristics and film modification of jets. In this paper, we compared the discharge characteristics and the film modifications of atmospheric pressure plasma jets with needle-ring electrode (NRE) and double-ring electrode (DRE). The results show that jet with NRE has stronger electric field intensity and higher discharge power, making it present more reactive oxygen particles and higher electron temperature, but its discharge stability is insufficient. In contrast, the jet with DRE has uniform electric field distribution of lower field intensity, which allows it to maintain stable discharge over a wide range of applied voltages. Besides, the modification results show that the treatment efficiency of PET film by NRE is higher than that by DRE. These results provide a suitable atmospheric pressure plasma jets device selection scheme for polymer film processing process.

Keywords: atmospheric pressure plasma jet, electrode structure, jet characteristics, modification

PACS: 52.25.–b, 52.50.Dg, 81.65.–b **DOI:** 10.1088/1674-1056/ace768

1. Introduction

In recent years, atmospheric pressure plasma jets (APPJ) have garnered significant attention in materials processing, owing to their pivotal role in material surface modification, etching, and film deposition.[1–10] Li *et al.*[11,12] investigated mechanisms of APPJ plume formation and morphology transition by electrical and spectral measurements as well as fast photography. An APPJ can generate a plasma plume that propagates away from the confinement of electrodes and into the ambient atmosphere. Abundant active species in the plasma plume can therefore be delivered to a location separated from the plasma generation zone. Compared to conventional plasma technology, atmospheric pressure plasma boasts of simple equipment, low power consumption, and the ability to operate stably at atmospheric pressure.[11,12] APPJ overcomes the discharge gap limitations of plate dielectric barrier discharge plasma and generates a large number of active particles, such as ions, electrons, and free radicals, in open space. These particles treat material surfaces directly without special requirements.[2] Therefore, APPJ exhibits great potential for application in the field of polymer film processing. The unique characteristics of APPJ highlight its significance in materials processing, making it a viable candidate for further research and development.

Polyethylene terephthalate (PET) film is a thin, light, and flexible polymer film widely used in the fields of electronics and medical applications due to its excellent electrical insulation, physical and mechanical properties. However, the low surface energy of PET films leads to unsatisfactory hydrophilicity, adhesion, and printability in industrial applications. Therefore, surface modification is often required to increase the surface free energy of PET films while maintaining their other properties, in order to improve their hydrophilicity and adhesion.[13,14]

Polymer films are commonly used in various applications, and surface modification is often necessary to improve their properties. APPJ sources have been widely used for this purpose, with different types of devices available based on the electrode structure. The most common ones include single-rod electrode,[11,12,15,16] rod-ring (or needle-ring),[4,6,10,17] single-ring,[18] and double-ring.[5,7,8,19] APPJ devices, all of which have been used by researchers for surface modification of polymer films. For example, Chen *et al.* used a double-ring APPJ device to enhance the surface electrical strength of epoxy resin samples by ionizing a mixture of He/CF_4 gas.[1] Zhou *et al.* used a homemade rod-ring APPJ device to optimize the cell adhesion and proliferation ability on the surface of poly (L-lactic acid) fiber membranes.[4] Baniya *et al.* used

†Corresponding author. E-mail: wangxingquan@gnnu.edu.cn
© 2023 Chinese Physical Society and IOP Publishing Ltd

a double-ring APPJ device for polypropylene material to improve its hydrophilicity.[5] However, there are differences in the discharge mechanism and the characteristics of the plasma jets generated by these devices due to their different electrode structures, leading to variations in the treatment results. Therefore, it is crucial to select the appropriate APPJ device for surface modification according to different needs in polymer film processing applications. This distinction is more conducive to the development of electronics and medical applications in related fields. Therefore, it is essential to explore the treatment effect and applicable scenarios of different types of APPJ sources.

In this paper, two types of devices with different electrode structures were used to generate APPJ, which were the needle-ring electrode (NRE) and the double-ring electrode (DRE). Furtherly, the effects of different electrode structures on the jet were investigated by electrical characteristics, optical characteristics, and electron excitation temperature. The discharge intensity of APPJ source is usually judged by electrical characteristics, including excitation voltage, current spike, and dissipated power. Optical characteristics include optical emission spectrum and spectral intensity analysis, which are used to reveal the presence of reactive species and the variation of spectral intensity in APPJ. Then, the effect of two types of APPJ on the surface modification of PET films was also investigated. Lastly, this paper explored the discharge mechanism of different electrode structures, and provided a suitable APPJ device selection scheme for polymer film processing process.

2. Experimental setup and diagnostic methods

2.1. APPJ source

Two self-developed APPJ devices shown in Fig. 1 were used in the experiments. The electrode of NRE consists of a stainless-steel capillary needle with an inner diameter of 0.24 mm and an outer diameter of 0.46 mm and a copper ring with a thickness of 0.1 mm and a width of 5 mm. The stainless-steel capillary needle is used as the high-voltage electrode, while the copper ring is wrapped around the outer wall of a quartz glass tube with an inner diameter of 0.5 mm and an outer diameter of 1 mm as the grounded electrode. The distance of the high-voltage electrode and the grounded electrode from the quartz glass tube nozzle are 18 mm and 3 mm, respectively, as shown in Fig. 1(a). The DRE consists of a high-voltage electrode copper ring, a grounded electrode copper ring, and a quartz glass tube as shown in Fig. 1(b). It is worth noting that the dimensions of both the copper ring and the quartz glass tube of DRE are the same as those of the NRE, and the distances between the two electrodes and the nozzle are also the same as the former. The position of collecting optical emission for OES measurements is located at the center point between the two electrodes, as shown in Fig. 1.

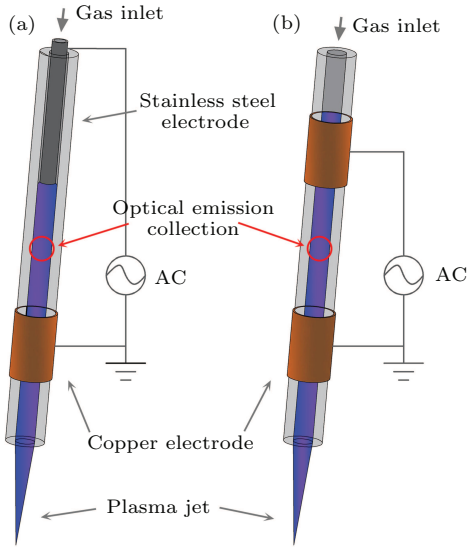


Fig. 1. Schematic diagrams of experimental setup with (a) needle-ring electrode (NRE) structure and (b) double-ring electrode (DRE) structure.

2.2. Diagnostic methods

In the experiments, argon (Ar, 99.99%) gas and oxygen (O_2, 99.99%) gas were used as working gases. Among them, the adjustable flow rate ranges of Ar and O_2 are 0–2 standard litre per minute (slm) and 0–100 standard cubic centimeter per minute (sccm), separately. The driving power supply of the APPJ adopts the high frequency plasma power supply (CTP-2000K; Nanjing Suman Electronics Co., Ltd.) with an output voltage range of 0 kV–30 kV and a frequency adjustment range of 5 kHz–20 kHz.

The applied voltage and discharge current of the jets were measured using a 1:1000 high-voltage probe (P6015A; Tektronix Inc.) and a current probe (P6021; Tektronix Inc.), respectively. The discharge waveforms were displayed and recorded by a digital oscilloscope (TDS2024C; Tektronix Inc.). The Lissajous plot method was used to measure the dissipated power with a capacitance of 10 nF, and the dissipated power was calculated according to the following equation:[19]

$$P = f \times \int (t) I(t) \mathrm{d}t, \tag{1}$$

where f is the discharge frequency, $V(t)$ and $I(t)$ are the voltage and the current of the discharge. In order to ensure the accuracy of the results, the average value was calculated from the results of multiple experiments to obtain the dissipated power. The optical emission spectra were collected using a spectrometer (SE2030-010-FUV; OTO Photonic Inc.) with a spectral wavelength range of 180 nm–850 nm. In addition, a contact angle meter (JY-PHb) was used to detect the water contact angle (WCA) on the polymer film surface. A drop of water with the volume of 2 μL was employed at the center of the treated regions, and the affinity of the drop to the film surface was

measured by a digital camera (DLC131-L) at the fixed position.

To investigate the impact of different electrode structures on the initial electric field distribution of the APPJ, this study employed physical field simulation software to establish two-dimensional axisymmetric simulation models. The electrostatic field module was utilized to calculate and solve the initial electric fields of two APPJ devices. The simulation software adopted the finite element method to numerically simulate the electrostatic field simulation region, utilizing triangular mesh as the mesh division type. The simulation method used for the initial electric field in this study is similar to that used in the paper by Wang *et al.*[8]

3. Results and discussion

3.1. Electrostatic field simulation

The longitudinal cross-sectional spatial distribution of the initial electric fields of NRE and DRE are presented in Figs. 2(a) and 2(b), respectively. The parameters of the electrodes and quartz glass tube are the same as in Fig. 1. Set the boundary conditions: terminal (high-voltage electrode boundaries) voltage $U_{\mathrm{HV}} = 5$ kV, ground (grounded electrode boundaries) voltage $U_{\mathrm{Gound}} = 0$ kV, space boundaries were zero charge. In this study, we have simplified the investigation of electric field distribution in the plasma jet, as it is composed of an electrostatic or Laplace electric field combined with a space charge electric field at the jet front in actual situation.[8,20] As a result, our simulation results solely present the initial electric field of two different types of APPJ and not the actual electric field. Thus, the simulation results presented in this section serve the purpose of qualitatively comparing the electrostatic field distributions of two electrode structures under the same conditions and providing a reference for the analysis subsequent experiments.

According to the simulation results as shown in Fig. 2, the electric field amplitude of NRE is up to 16.2 kV/mm of the plasma source, while the maximum of DRE is only 5.03 kV/mm, which shows that the maximum electric field intensity of NRE is about 3.2 times that of DRE.

According to the legend in Fig. 2(a), it can be seen that the maximum electric field intensity of NRE is located around the tip of the high-voltage electrode. Taking the vertical coordinate $r = 0.23$ at the tip edge point of the high-voltage electrode as the reference, a line is drawn along the parallel direction of the quartz tube, and the electric field intensity along the line inside the NRE and DRE quartz tubes are shown in Fig. 3. Obviously, the electric field distribution between the two electrodes of NRE is extremely non-uniform. Specifically, the electric field intensity reaches a maximum near the tip of the high-voltage electrode, and diminishes rapidly along the radial direction, reaching its minimum at the midpoint between the two electrodes, before rising again. In contrast, the electric field distribution of DRE is relatively even, symmetrical to the center point between the two electrodes. Although the electric field intensity in DRE experiences a sudden change at both edges of the electrodes, its maximum value is substantially lower than that of NRE.

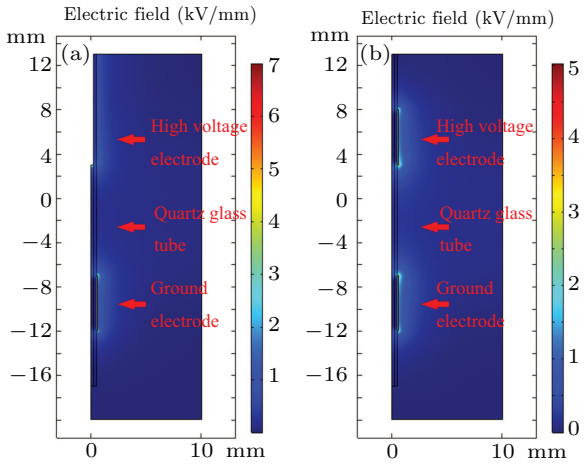


Fig. 2. Simulation results of the electric filed for the APPJs with (a) NRE and (b) DRE.

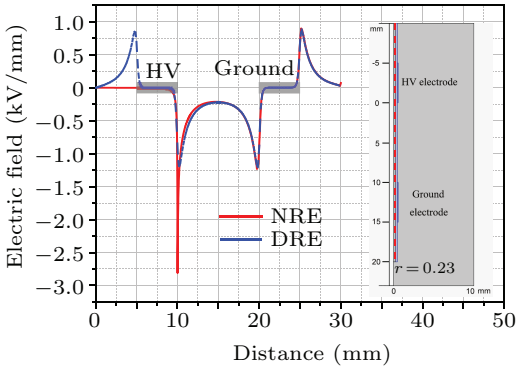


Fig. 3. The distribution of electrical field intensity inside the quartz tube with the red line. HV: high voltage electrode. Ground: ground electrode.

3.2. Electrical characteristics

As the applied voltage gradually increases from zero to a specific value, a plasma jet abruptly generates within the quartz tube. This voltage required to initiate the plasma jet is referred to as the excitation voltage.[8] At the working gas Ar flow rate of 500 sccm and an applied voltage frequency of 9 kHz, the excitation voltages of NRE and DRE are 4.16 kV and 4.24 kV, respectively, as depicted in Fig. 4(a). With the increase of O_2 flow rate from 0 sccm to 25 sccm, both NRE and DRE show an increase in excitation voltage. Notably, DRE consistently exhibits larger excitation voltages than NRE under identical conditions. Oxygen is an electronegative gas that can absorb electrons through the attachment processes to produce negative ions, leading to electron consumption within the discharge.[3,19] Therefore, when the O_2 content increases during discharge, a greater applied voltage is necessary to supply an adequate number of electrons to initiate and maintain

the APPJ. Combined with the electrostatic field simulation results, the local electric field strength inside the NRE quartz tube is higher than that of the DRE. As a result, the gas present within the discharge zone of NRE tube is more prone to ionization, which facilitates the generation of APPJ at lower voltage. Conversely, DRE requires higher voltage due to its relatively lower electric field intensity.

The discharge voltage and current waveforms of NRE and DRE were shown in Figs. 4(b) and 4(c), respectively, when pure Ar was used as the working gas at a flow rate of 500 sccm, with an applied voltage frequency of 8.5 kHz and voltage magnitude of 6.5 kV. Notably, the current waveform of NRE displays a single intense spike during each positive half cycle of the applied voltage with the largest peak value of about 432 mA, whereas DRE exhibits multiple relatively weak but uniform and stable current spikes during each positive and negative half cycles of the applied voltage, with the largest peak value of approximately 352 mA. This can be attributed to the high-voltage electrode of NRE being exposed inside the quartz tube and in direct contact with the plasma during discharge, while the electrode structure of DRE is symmetrical, and there is a quartz dielectric layer between the electrode and the plasma. Additionally, electrostatic field simulation results showed that there is an intense local electric field near the high-voltage electrode of NRE, which can provide a large number of electrons for the ignition of the plasma. While the electric field of DRE is symmetrical and weak, so only a small number of electrons accumulate on the surface of the quartz tube near the two electrodes. Therefore, the electrode structure could greatly affect the electrical characteristics of the plasma. For NRE, the extremely nonuniform electric field distribution tends to form intense current spikes. And the uniform electric filed distribution generated by the DRE makes the discharge more even and form multiple smaller amplitude current spikes. In addition, the electric field of the needle electrode of NRE is mainly concentrated near the tip, which results in only a small number of current pulses forming at the same location during a positive voltage cycle. The ring electrode of DRE has a width, and the electric field distribution near the electrode is not uniform,[21] which means that discharge will occur at different positions on the inner surface of the dielectric layer during different times of a positive voltage cycle. As the external voltage increases, the charges accumulated on the inner surface of the dielectric layer successively form multiple current pulses. Therefore, the number of current pulses for DRE is much more than that for NRE.

The dissipated power is a crucial factor affecting the electrical characteristics of APPJ with different electrode structures and also need to be considered in the practical application of APPJ. It can be calculated using Eq. (1), and figure 4(d) shows the power variation with applied voltage for NRE and DRE. Both NRE and DRE exhibit an increasing power trend with applied voltage, but with different voltage ranges. Specifically, we observed that APPJ could only be sustained in the 5.5 kV to 6.5 kV range for NRE, beyond which it would transition to an arc discharge accompanied by a loud current sound. This is mainly caused by the intense local electric field of NRE, which allows it to generate and maintain APPJ at lower voltages. For DRE, it requires a higher voltage to initiate APPJ, and its power rises continuously in the voltage range of 6.5 kV to 9 kV. The uniform and lower intensity electric field makes it less prone to arc discharge. The dissipated power results of the APPJ with two different electrodes confirmed that the discharge of NRE was more intense than that of DRE.

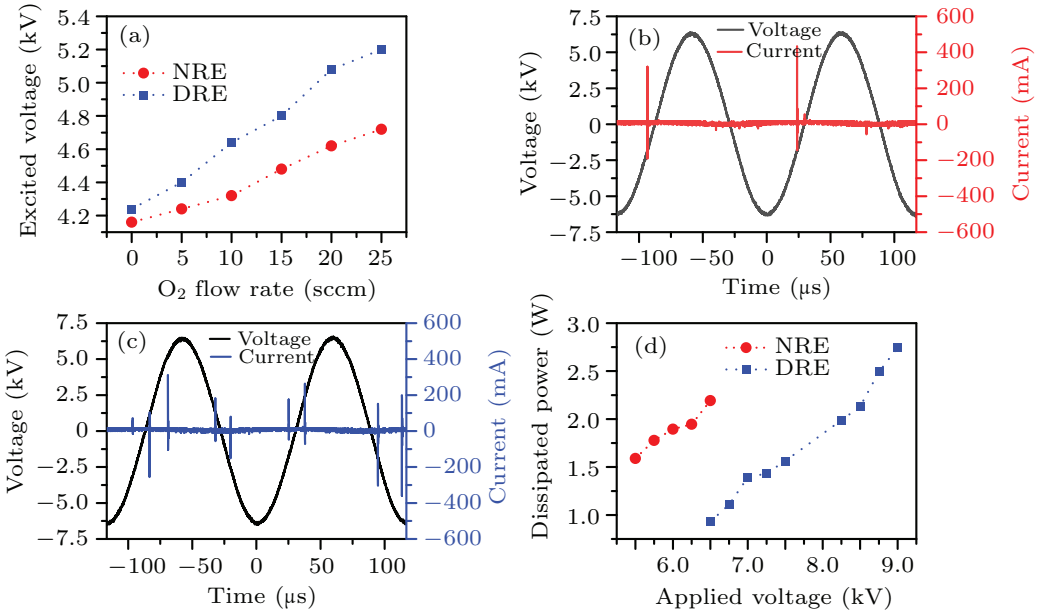


Fig. 4. The electrical characteristics of APPJs with (a) excitation voltages of two different electrode structures with different O_2 flow rates, the waveforms of voltage and current for (b) NRE, (c) DRE, and (d) the dissipated power variation with applied voltage.

3.3. Optical characteristics

Optical emission spectrum (OES) is utilized to detect the chemical species present in APPJ. The emission spectra in the range of 250 nm to 850 nm, obtained in Ar/O_2 plasma jet for two different types of APPJ, with an applied voltage frequency of 8.5 kHz, a dissipated power of 1.9 W, and Ar flow rate of 500 sccm, are shown in Fig. 5. Figures 5(a) and 5(b) show the emission spectra of NRE at added O_2 flow rate of 20 sccm and 40 sccm, respectively, while figure 5(c) exhibits the emission spectra of DRE at an added O_2 flow rate of 20 sccm. It is evident that the excited species present include OH ($A^2\Sigma^+ \rightarrow X^2\Pi$) at 309.1 nm, N_2 second positive band ($C^3\Pi \rightarrow B^3\Pi$), O at 777.4 nm and 844.6 nm, and intensive argon lines in the range from 680 nm to 850 nm. As the plasma is generated at atmospheric pressure, impurities such as N_2, H_2O, and O_2 present in the air can easily mix into the working gas. In this experiment, the working gas is an Ar/O_2 mixture, the Ar metastables and electrons generated in the discharge collide with impurities in the gas, resulting in a variety of excited species observed in the emission spectra.[22,23] The atomic O in APPJ is mainly produced through the collision of oxygen molecules with electrons or Ar metastables ($e + O_2 \rightarrow O(3p^5P) + O + e$, $Ar^* + O_2 \rightarrow O(3p^5P) + O + Ar$),[24] and the presence of the OH radical is attributed to the dissociation of water molecule ($e + H_2O \rightarrow e + H + OH$, $Ar^* + H_2O \rightarrow OH + Ar + H$).[19,24] These reactive oxygen species (ROS) are strongly oxidizing and play a crucial role in various applications such as materials processing and biomedical processes.[25]

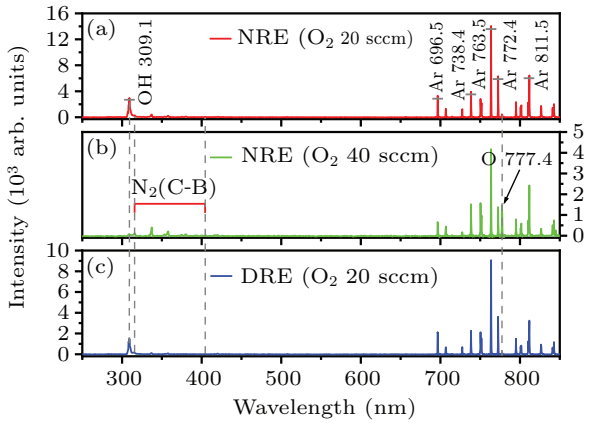


Fig. 5. OES of APPJ generated by NRE with the O_2 flow rate of (a) 20 sccm, (b) 40 sccm, and (c) DRE with the O_2 flow rate of 20 sccm.

The optical emission spectral intensity of OH (309.1 nm), Ar (763.5 nm), O (777.4 nm), and O (844.6 nm) radicals in the OES of NRE and DRE are shown in Figs. 6(a) and 6(b), respectively, as the function of added O_2 flow rate. It can be seen that the intensity of the O atoms (777.4 nm, 844.6 nm) in the plasma rises with O_2 flow rate when the working gas is doped with a small amount of O_2 (content of 0%–7.4%), with the optimal O_2 content being 7.4% in this experiment. However, the intensity of the O atoms decreases as the O_2 flow rate beyond 40 sccm (content $>$ 7.4%). In the Ar/O_2 plasma jet, O atoms are primarily generated via electron dissociation of oxygen molecules and Penning ionization of oxygen molecules with Ar metastables.[24] Properly adjusting the flow rate of O_2 can increase the number of O atoms. The electronegativity of O_2 causes electron attachment in the discharge, which consumes electrons to produce negative ions.[3,19] This process competes with the collision of oxygen molecules with electrons. At O_2 flow rates below 40 sccm, collision dominates in the discharge and the attachment process has little effect on electron consumption and the generation of Ar atoms and metastables. However, as the O_2 flow rate is equal to 40 sccm, the intensity of Ar atoms starts to decrease while the intensity of O atoms reaches its peak. Consequently, as the O_2 flow rate exceeds 40 sccm, the intensities of both O atoms and Ar (763.5 nm) atom decrease sharply. This can be attributed to the enhancement in electron attachment, which consumes more electrons during the formation of negative ions. There is a reduction in the number of electrons available for collision with O_2 and Ar, ultimately suppressing the production of O atoms and Ar metastables. The trend of OH (309.1 nm) radical production is consistent with that of Ar atoms as shown in Fig. 6.

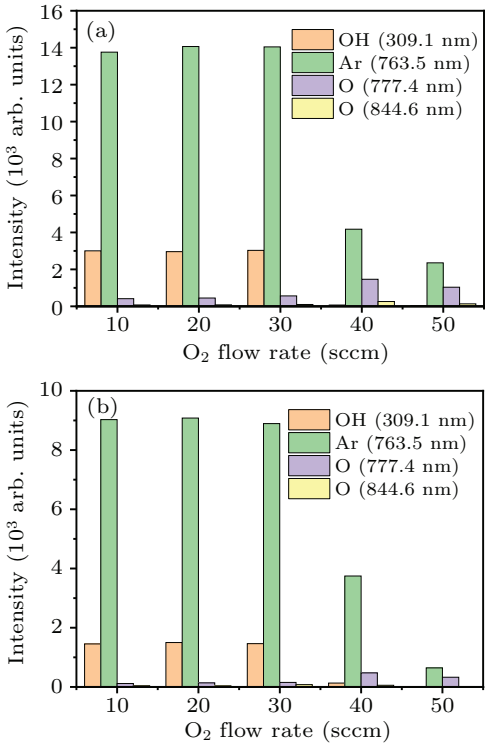


Fig. 6. Spectral intensity of OH at 309.1 nm, Ar at 763.5 nm, O atoms at 777.4 nm and 844.6 nm in the plasma generated by (a) NRE and (b) DRE with different O_2 flow rates.

In summary, it is evident that the reaction system in APPJ is complex during O_2 flow rate variation. Various reactions

such as electron collision and electron attachment of electronegative gas work jointly to determine the formation of excited species. Notably, the highest efficiency of active O atoms production was observed at the O_2 flow rate of 40 sccm in this experiment.

The relationship between the variation of the O (777.4 nm) atom spectral intensity in the plasma generated by NRE and DRE with the O_2 flow rate is presented in Fig. 7. The trends in intensity variation of O atoms are similar in both cases, with the highest generation efficiency of O atom achieved at the O_2 flow rate of 40 sccm. Moreover, the APPJ of NRE exhibits higher relative intensities of O atoms than the DRE under all conditions, indicating its stronger oxidation characteristics. This finding further confirms the greater electric field intensity in APPJ of NRE compared to DRE, as observed in the electrostatic field simulation.

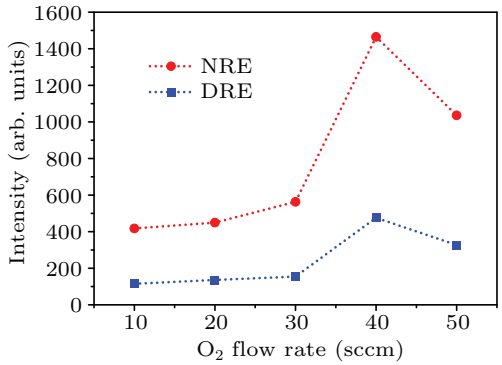


Fig. 7. The variation of the O (777.4 nm) atom spectral intensity in the plasma generated by NRE and DRE with different O_2 flow rates.

3.4. Electron excitation temperature

Crucial parameters of APPJ, including electron excitation temperature (T_{exc}), can be calculated by OES results, as fiber optic devices used in optical diagnostics exhibit low sensitivity to the electromagnetic field generated by APPJs.[26]

To ensure the accuracy of the T_{exc} calculation of APPJ, we selected several characteristic atomic Ar spectral lines (750.4 nm, 794.8 nm, 811.5 nm, 826.5 nm, 842.5 nm) from the OES for the Boltzmann plot method. The calculation equation is as follows:[27,28]

$$\ln\left(\frac{I_i\lambda_i}{g_iA_i}\right) = -\frac{E_i}{kT_{exc}} + C, \tag{2}$$

where I_i is the atomic emission intensity, λ_i is wavelength of spectral lines, A_i and g_i are the transition probability and degeneracy of different energy levels, respectively, and k is the Boltzmann constant. The parameters of the characteristic atomic Ar spectral lines used for the calculation are list in Table 1.[3,27]

The Boltzmann plot of atomic Ar spectral lines of at the O_2 flow rate of 30 sccm is shown in Fig. 8(a), and figure 8(b) displays the variation of T_{exc} for both NRE and DRE with O_2 flow rate. The results indicate that the T_{exc} of NRE and DRE range from 0.336 eV to 0.455 eV and 0.305 eV to 0.410 eV, respectively. A slight increase in T_{exc} is observed for both when the O_2 flow rate is increased from 10 sccm to 30 sccm. This increase can be attributed to the increase in discharge voltage caused by the electronegativity of O_2, which enhances the electric field intensity of APPJ. As a result, the mean electron kinetic energy increases, resulting in an increase of T_{exc}.[29,30] However, the variation of T_{exc} is small due to the relatively low percentage of O_2 in the gas mixture and electron collision dominates in the discharge. At O_2 flow rates of 40 sccm or greater, T_{exc} decreases rapidly due to the enhanced electron attachment of O_2,[19] which reduces the number of electrons available for collision in APPJ. This finding is supported by the variation of the intensities of Ar atoms and OH radicals, as shown in Fig. 6. T_{exc} derived from Boltzmann plot is a rough approximation of the electron temperature (T_e) under atmospheric pressure.[29,31] It is evident that, under the same conditions, T_e of APPJ generated by NRE and DRE varies similarly with the addition of O_2 flow rate, while the T_e of APPJ generated by NRE is higher than that of DRE, indicating stronger chemical characteristics of NRE than DRE.

Table 1. The data of selected argon spectral lines.

λ (nm)	A (10^7 s^{-1})	g	E (eV)
750.4	4.5	1	13.47989
794.8	1.86	3	13.28265
811.5	3.3	7	13.07572
826.5	1.53	3	13.32786
842.5	2.15	5	13.09488

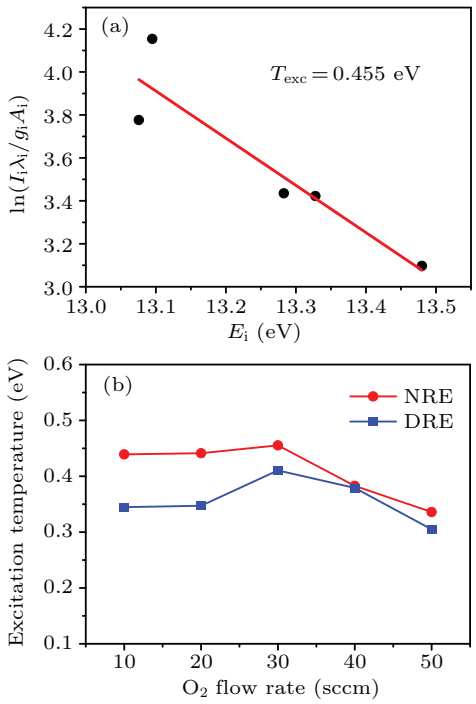


Fig. 8. (a) Boltzmann plot of argon lines (750.4 nm, 794.8 nm, 811.5 nm, 826.5 nm, 842.5 nm) with the O_2 flow rate of 30 sccm and (b) the electron excitation temperature of APPJ generated by NRE and DRE with different O_2 flow rates.

3.5. PET surface treatments

To further investigate the differences between two types of APPJs, both were employed for surface modification of PET films. The effect of APPJs with different electrode structures on the treatment outcomes was evaluated by analyzing the variation of hydrophilicity on the PET surface. Commercial PET films with thickness of 50 μm and permittivity of 3.8 were used for treatments. The films are uniformly sized to 1.5 mm×1.5 mm and positioned on a quartz glass substrate with a permittivity of 3.8. The experimental parameters comprised an applied voltage frequency of 8.5 kHz, dissipated power of 1.9 W, Ar flow rate of 500 sccm, O_2 flow rate of 40 sccm, distance between device nozzle and sample of 7 mm or 10 mm, and various treatment times (10 s, 15 s, 30 s, 60 s, and 90 s). In all the treatment times, the temperature of APPJs did not rise obviously. The variation of WCA on the PET surfaces as a function of treatment time using NRE is presented in Fig. 9(a). The WCA decreased to 26.9° when film was treated 90 s. The ROS particles, showed in Fig. 5, such as OH radicals and O atoms can break chemical bonds (C–C or C–H, etc.) on the PET surface, resulting in the formation of macromolecular radicals. Subsequently, the macromolecular radicals combine with ROS particles to generate oxygen-containing polar groups (C–O or C=O, etc.) on the film surface, thus enhancing the hydrophilicity of the PET film through the incorporation of the polar groups.[2,32]

Figure 9(b) shows the variation of the WCA on the PET surface as a function of treatment times for NRE and DRE with different nozzle-to-sample distances. At a distance of 10 mm, the WCA exhibited a sharp decrease within the first 10 s, with change rates of 38.9% and 29.6% for NRE and DRE, respectively. After 90 s of treatment, the WCAs decreased to 27.0° and 29.9°, respectively. These results indicate that both APPJ exhibit similar treatment trends, but NRE is more efficient than DRE. By adjusting the distance to 7 mm, the WCA change rates for both NRE and DRE increased to 54.9% and 50.2%, respectively, within the first 10 s of treatment. After 90 s of treatment, both WCAs approached 27.0°. It can be seen that decreasing the distance of nozzle-to-sample facilitates more efficient contact between the ROS particles and the sample, leading to improved treatment efficiency. At a given treatment time, NRE exhibits higher treatment efficiency than DRE, but ultimately DRE can achieve a similar treatment effect as NRE. OES and T_{exc} results of APPJ indicate that NRE has a greater concentration of O atoms, which results in stronger oxidation characteristics and enables it to treat PET surfaces more efficiently than DRE per unit time. As discussed in the electrical characteristic subsection, NRE can obtain higher discharge intensity of APPJ at lower voltages, but is more prone to transitioning to arc discharge. The high temperature plasma generated by arc discharge may damage polymer films during treatment, while DRE can maintain stable discharge over a wide range of applied voltage. In general, the discharge intensity and chemical characteristics of APPJ are influenced by the electrode structure, which ultimately affects efficiency of PET surface treatment. Both kinds of APPJ have good treatment effect on improving the hydrophilicity of PET film. Among them, APPJ with NRE has stronger discharge intensity and its treatment efficiency is slightly higher than that of DRE, while APPJ with DRE is more stable and more suitable for continuous and stable surface modification.

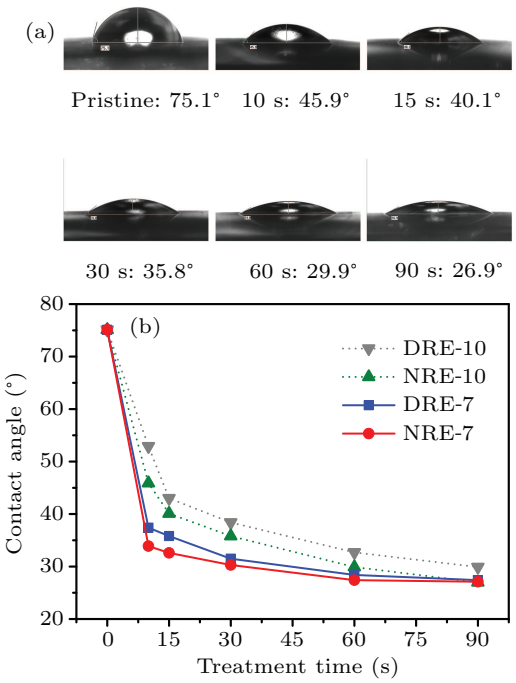


Fig. 9. (a) The photos of PET surface WCA with treatment time using NRE and (b) the variation of PET surface WCA as a function of treatment time for NRE and DRE with different nozzle-to-sample distances.

4. Conclusion

This paper discussed the discharge mechanism and the characteristics of Ar/O_2 APPJ with two different kinds of electrode structures and their effects on surface modification of PET films. Electrostatic field simulation results showed that NRE exhibits an extremely asymmetric electric field distribution and high field intensity, which provides more electrons for the generation of APPJ. In contrast, APPJ with DRE displays a more uniform electric field distribution with lower field intensity. The electrical characteristics results show that to obtain the same dissipated power of APPJ, NRE requires a lower voltage than DRE, but it has a narrower range of applied voltage range and is prone to transition to arc discharge, while DRE can maintain stable APPJ at higher voltages. OES and T_{exc} results presented that both APPJs contain multiple ROS particles, such as O (777.4 nm). The production of ROS was affected by the flow rate of O_2, with the intensity of O atoms peaking at an O_2 flow rate of 40 sccm due to competition between electron collision processes and electron attachment processes. The intensity of O atoms and T_e of NRE was found

to be higher than those of DRE under the same conditions, indicating that APPJ with NRE has stronger chemical oxidation characteristics. PET surface treatments showed that both APPJ exhibited similar treatment trends, but NRE was more efficient than DRE. NRE has stronger discharge intensity and its treatment efficiency is slightly higher than that of DRE, while DRE is more stable and more suitable for continuous and stable surface modification. This study provides valuable insights for selecting the appropriate APPJ with different electrode structures for polymer film processing applications.

Acknowledgements

Project supported by the National Natural Science Foundation of China (Grant No. 11565003), the Jiangxi Province Academic Degree and Postgraduate Education and Teaching Reform Research Project (Grant No. JXYJG-2022-180), and the Scientific Research Base Project of Gannan Normal University (Grant No. 22wdxt01).

References

[1] Chen S L, Cheng T, Chen Z Q, Chen X Y and Zhang G J 2021 *Appl. Surf. Sci.* **544** 148956
[2] Sasmazel H T, Alazzawi M and Alsahib N K A 2021 *Molecules* **26** 1665
[3] Fang Z, Shao T, Wang R X, Yang J and Zhang C 2016 *Eur. Phys. J. D* **70** 79
[4] Zhou S N, Wen L, Tian Z H, Yan K C, Cheng J J, Xia L J, Wang H, Chu J R and Zou G 2020 *Vacuum* **182** 109763
[5] Baniya H B, Guragain R P, Baniya B and Subedi D P 2020 *Int. J. Polym. Sci.* **2020** 3860259
[6] Nakazawa K, Yamamoto S, Nakagawa E, Ogino A, Shimomura M and Iwata F 2020 *Aip Adv.* **10** 095103
[7] Wang T, Wang J H, Wang S Q, Lv L, Li M and Shi L P 2021 *Appl. Surf. Sci.* **570** 151258
[8] Wang T, Wang S Q, Wang J H, Chen S L, Li M, Shi L P and Zhang X Q 2021 *Plasma Process Polym.* **19** 2100139
[9] Banerjee S, Adhikari E, Sapkota P, Sebastian A and Ptasinska S 2020 *Materials* **13** 2931
[10] Yamamoto S, Nakazawa K, Ogino A and Iwata F 2022 *J. Micromech. Microeng.* **32** 015006
[11] Li X C, Chen J Y, Lin X T, Wu J C, Wu K Y and Jia P Y 2020 *Plasma Sources Sci. Technol.* **29** 065015
[12] Li X C, Chen J Y, Wu K Y, Wu J C, Zhang F R, Zhao N, Jia P Y, Yin Z Q, Wang Y J and Ren C H 2021 *Phys. Plasmas* **28** 103507
[13] Zhang Y, Ishikawa K, Mozetič M, Tsutsumi T, Kondo H, Sekine M and Hori M 2019 *Plasma Processes Polym.* **16** 1800175
[14] Sirotkin N, Khlyustova A, Titov V and Agafonov A 2020 *Plasma Processes Polym.* **17** 2000012
[15] Wu S Q, Lu X P, Xiong Z L and Pan Y 2010 *IEEE Trans. Plasma Sci.* **38** 3404
[16] Chen J Y, Zhao N, Wu J C, Wu K Y, Zhang F R, Ran J X, Jia P Y, Pang X X and Li X C 2022 *Chin. Phys. B* **31** 065205
[17] Chen Z Q, Zhou B K, Zhang H, Hong L L, Zou C L, Li P, Zhao W D, Liu X D, Stepanova O and Kudryavtsev A A 2018 *Chin. Phys. B* **27** 055202
[18] Yoshiki H and Saito T 2008 *J. Vac. Sci. Technol. A* **26** 338
[19] Asghar A H and Galaly A R 2021 *Appl. Sci.* **11** 6870
[20] Robert E, Darny T, Dozias S, Iseni S and Pouvesle J M 2015 *Phys. Plasmas* **22** 122007
[21] Mangolini L, Orlov K, Kortshagen U, Heberlein J and Kogelschatz U 2002 *Appl. Phys. Lett.* **80** 1722
[22] Zhang Q, Sun P, Feng H Q, Wang R X, Liang Y D, Zhu W D, Becker K H, Zhang J and Fang J 2012 *J. Appl. Phys.* **111** 123305
[23] Shao X J, Zhang G J, Zhan J Y and Xu G M 2011 *IEEE Trans. Plasma Sci.* **39** 3095
[24] Jin Y, Ren C H, Yang L and Zhang J L 2016 *Plasma Sci. Technol.* **18** 168
[25] Yonemori S and Ono R 2014 *J. Phys. D: Appl. Phys.* **47** 125401
[26] Bruggeman P and Brandenburg R 2013 *J. Phys. D: Appl. Phys.* **46** 464001
[27] Zhang H B, Yuan F L and Chen Q 2020 *IEEE Trans. Plasma Sci.* **48** 3621
[28] Yin G Q, Wang J J, Gao S S, Jiang Y B and Yuan Q H 2021 *Chin. Phys. B* **30** 095204
[29] Joh H M, Choi J Y, Kim S J, Chung T H and Kang T H 2014 *Sci. Rep.* **4** 6638
[30] Léveillé V and Coulombe S 2005 *Plasma Sources Sci. Technol.* **14** 467
[31] Li X C, Lin X T, Wu K Y, Ren C H, Liu R and Jia P Y 2019 *Plasma Sources Sci. Technol.* **28** 055006
[32] Demaude A, Inturri R, Satriano C, Leroy P and Reniers F 2021 *Plasma Process Polym.* **18** 2100005